ACS OMEGA

http://pubs.acs.org/journal/acsodf

Article

Phytosynthesis of Co_3O_4 Nanoparticles as the High Energy Storage Material of an Activated Carbon/Co_3O_4 Symmetric Supercapacitor Device with Excellent Cyclic Stability Based on a Na_2SO_4 Aqueous Electrolyte

Badreah Ali Al Jahdaly, Ahmed Abu-Rayyan, Mohamed M. Taher,* and Kamel Shoueir*

Cite This: *ACS Omega* 2022, 7, 23673−23684

Read Online

ACCESS | Metrics & More | Article Recommendations

ABSTRACT: The benign preparation of cobalt oxide nanoparticles (Co_3O_4-NPs) was performed using marine red algae extract (*Grateloupia sparsa*) as a simple, cost-effective, scalable, and one-pot hydrothermal technique. The nominated extract was employed as an environmental reductant and stabilizing agent. The resultant product showed the typical peak of Co_3O_4-NPs around 400 nm wavelength as ascertained by UV−vis spectroscopy. Size and morphological techniques combined with X-ray diffraction (XRD) showed the small size of Co_3O_4-NPs deformed in a spherical shape. The activated carbon (AC) electrode and Co_3O_4-NP electrode delivered a specific capacitance (C_{sp}) of 125 and 182 F g^{-1} at 1 A g^{-1}, respectively. The energy density of the AC and AC/Co_3O_4 electrodes with a power density of 543.44 and 585 W kg^{-1} was equal to 17.36 and 25.27 Wh kg^{-1}, respectively. The capacitance retention of designed electrodes was 99.2 and 99.5% after 3000 cycles. Additionally, a symmetric AC/Co_3O_4//AC/Co_3O_4 supercapacitor device had a specific capacitance (C_{sp}) of 125 F g^{-1} and a high energy density of 55 Wh kg^{-1} at a power density of 650 W kg^{-1}. Meanwhile, the symmetric device exhibited superior cyclic stability after 8000 cycles, with a capacitance retention of 93.75%. Overall, the adopted circular criteria, employed to use green technology to avoid noxious chemicals, make the AC/Co_3O_4 nanocomposite an easily accessible electrode for energy storage applications.

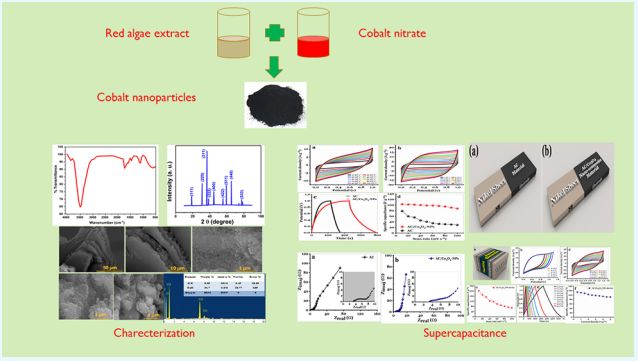

1. INTRODUCTION

Many scientists are developing various techniques to fabricate and optimize the synthesis of metals and metal oxide nanoparticles using environmentally green technologies.[1−3] These methods mainly rely on cost-effective precursors, safety, and saving preparation time. The mechanism of creating nanoparticles generated by green synthesis has yet to be established and understood due to the difficulty of synthesizing most nanoparticles using the bioprocess, including marine red algae.[3−7]

Marine algae (*Grateloupia sparsa*) naturally exist in large amounts and have become essential for the green synthesis of nanomaterials.[8,9] The remarkable influence of algae is related to their capability to reduce and stabilize most metal ions to their zero-valent nanoparticles (NPs), rendering them great challenges in the nanoparticle production.[1] Algae, given the presence of organic compounds, such as carbohydrates and polyphenols, act as reducing and stabilizing agents for the formation of nanoparticles. Currently, algae-capped and -stabilized cobalt oxide nanoparticles (Co_3O_4-NPs) have gained widespread attention, perhaps promoted by global environmental awareness driving the research toward sustainable strategies.[10−14] In transforming metal ions to nanoparticles of metals, metal oxides, or bimetallic metals, the natural material from algae behaves as both a capping and stabilizing agent. They could be intracellular or extracellular reactions, depending on the size of the NPs.[15]

Several applications aim to valorize green materials in a circular economy approach, such as supercapacitors or ultracapacitors, defined as energy-dense devices and balanced rate efficacy.[16,17] According to charge storage mechanisms, most of these devices are electrochemical double-layer capacitors and pseudocapacitors. Charge separation at the electrode−electrolyte interface is the source of capacitance in electrochemical

Received: April 13, 2022
Accepted: June 10, 2022
Published: June 28, 2022

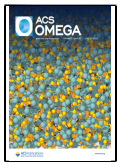

https://doi.org/10.1021/acsomega.2c02305
ACS Omega 2022, 7, 23673−23684

double-layer capacitors, predominantly carbon-based materials.[18] Pseudocapacitors, as previously stated, possess low conductivity, which prevents the rapid electron from transporting toward the high-rate capability.[19] As a result, new electrode materials should be created with all characteristics that lead to the most fantastic supercapacitor behavior, such as superior electrical conductivity, good rate capability, high porosity, and high capacitance.[20]

Transition metal oxides have recently been encouraged by the high theoretical specific capacitance.[21] These transition metal oxides like cobalt oxides [mainly cobalt (II) oxide (CoO) and cobalt (II, III) oxide (Co_3O_4)] have been extensively investigated as the supercapacitor electrodes owing to their enhanced theoretical capacity. Co_3O_4-NPs are transition metal oxides that serve as effective p-type semiconductors.[22,23] Catalysis, electrochromic devices, magnetic resonance imaging (MRI), drug delivery, gas sensors, lithium batteries, and energy storage are possible applications of Co_3O_4-NPs that may be considered.[24−26]

Due to its unique features, Co_3O_4 may be a viable alternative to the more expensive RuO_2, which is widely desired as the electrochemically active material in electrochemical capacitors.[27] Recently, microwave-heated synthesis of Co_3O_4 nanoparticle-embedded graphene nanosheets was raised. In a 5 M KOH electrolyte, the resulting composite had a specific capacitance of 242.1 F g^{-1} (scan rate: 10 mV s^{-1}).[28] Also, a needle-shaped Co_3O_4/graphene composite was hydrothermally synthesized and demonstrated a maximum capacitance of 157.7 F g^{-1} at a current density of 0.1 A g^{-1} in a 2 mol L^{-1} KOH solution.[29] AuNPs decorated with Co_3O_4NPs exhibit a specific capacitance of 681 F g^{-1} higher than that of pristine Co_3O_4 of 368 F g^{-1}; in addition to this, many studies have been conducted on the application of Co_3O_4 in supercapacitors.[30−32]

One-pot synthesis was a critical issue since Co_3O_4-NPs were prepared with a size of around 12 nm, and the maximum capacitance of 346 F g^{-1} with cyclic stability did not exceed 1% degradation even after 1000 cycles.[33] The *Camellia sinensis* leaf extract was used as a stabilizing agent during the synthesis of Co_3O_4-NPs with an average grain size of 39 nm and consequently calcined at 800 °C. The electrochemical performance exhibited a relatively 138 F g^{-1} capacitance.[34] But in some cases, more considerable power, more energy, consuming time, and insufficient reducing character exist. In another approach, a sandwich-shelled hollow $TiO_2/Co_3O_4//Co_3O_4/C$ composite can also be created by sequentially coating Co_3O_4 nanosheets and TiO_2 particles on Co_3O_4/C hollow spheres. After 100 cycles at 0.2 A g^{-1}, the composite has a lithium storage capacity of 1081.78 mAh g^{-1} and 772.23 mAh g^{-1} after 300 cycles at 1 A g^{-1}.[35]

The present protocol matches the requirements of green chemistry in terms of utilizing sustainable species for motivated preparation of metal oxides complying with circular economy concepts. The current work exploits the ability to fabricate biodesigned tricobalt tetraoxide nanoparticles (Co_3O_4-NPs) from the *G. sparsa* extract rather than organic reagents for electrochemistry domains. The morphology, as well as electrochemical features of the materials, was characterized. In particular, carbon-mixed Co_3O_4-NPs are frequently employed in electrochemical applications because they have a high surface area and excellent electrical conductivity leading to an overall improvement in the detection limit (LOD) and sensitivity.

2. EXPERIMENTS

2.1. Materials and Reagents. Marine red algae were collected from the Mediterranean Sea in Alexandria, Egypt. The temperature of seawater was between 21.0 and 23.0 °C, and the measured pH was 7.7−8.4. Cobalt (II) nitrate hexahydrate ($Co(NO_3)_2{\cdot}6H_2O$) reagent grade, 98%, was purchased from Aldrich Chemical Co. Carbon black as a source of activated carbon (AC) (particle size 100 μm) was purchased from Indian Co; NaOH and ethanol (95%) were purchased from German Co; poly(vinylidene fluoride) with average M_w ∼180 000 and average M_n ∼107 000 was purchased from Aldrich Chemical Co. *N*-methyl-2-pyrrolidone (NMP) was provided by MERCK.

2.2. Methods. *2.2.1. Sampling of Marine Red Algae.* The collected red algae samples were picked up and washed with seawater to remove foreign particulates such as epiphytes and combined sand particles. The pieces were kept in an icebox and brought to the lab and then washed with running tap water followed by ethanol to remove the residual red color dye and their fish odor. They were dried on a blotting paper to remove excess water. The produced washed powder was subjected to drying for 48 h in the open air, and then, the massive amount of red algae powder was obtained by crushing the dried powder in a cape with a 400 wt model CH-174Q and kept in airtight plastic bottles before the next step.

2.2.2. Preparation of the Marine Red Algae Extract (G. sparsa). Under magnetic stirring, the as-prepared red algae powder (5 g) was added to 100 mL of double-distilled water (DDI) and submitted for boiling for 2 h at a controlled 80 °C. The obtained extraction was separated using nylon mash. A Whatman nylon membrane filter (0.45 μm, pore size) was used to filtrate the resultant extraction. Then, the extraction was centrifuged (SIGMA 2-16p benchtop centrifuge) at 8000 rpm for 10 min to remove any unvisual impurities, and the mixture was stored in a refrigerator at ambient temperature.

2.2.3. Synthesis of Tricobalt Tetraoxide Nanoparticles (Co_3O_4-NPs). In a typical experiment, 0.1 M $Co(NO_3)_2{\cdot}6H_2O$ was prepared in 50 mL of DDI. In the meantime, 50 mL of the prepared marine red algae extract was slowly added with vigorous stirring, and the temperature was maintained at 70 °C during the reaction. The appropriate dark brown color was seen in the mixture after 30 min from the first addition. Then, 0.01 M NaOH solution was added dropwise until the pH of the mixture was attained around 9.0. A yellow precipitate was developed and left to settle. Eventually, the residue was repeatedly washed with pure water and ethanol and dried overnight at 75 °C. The yield was then ground and calcined in a laboratory chamber furnace for 4 h at 450 °C.

2.2.4. Activated Carbon AC/Co_3O_4 Electrode Preparation. A current collector (Nickel sheet) was cut into a rectangular area of 1 × 2 cm^2, etched with ethanol, washed with running water for 3 min, and then dried in an oven (BINDER ED 23 Heating oven) for 10 min. AC, Co_3O_4, carbon black, and a binder poly(vinylidene fluoride) (PVDF) were mixed in a mass ratio of 51:30:10:9 using a mortar and pestle. The mixture was added to 0.3 mL of NMP as a solvent in an ultrasonic device to make a slurry with a homogeneous paste. The AC/Co_3O_4 slurry was deposited onto a nickel sheet of 1 cm^2 rectangular area and subsequently dried overnight at 60 °C. The mass for the AC/Co_3O_4 nanocomposite electrode was 2 mg on a 1 cm^2 area.

2.3. Characterization. *2.3.1. Characterization of Co_3O_4-NPs.* FTIR spectra was recorded using a Thermo Scientific Nicolet iS20 FTIR spectrometer to illustrate the organic

https://doi.org/10.1021/acsomega.2c02305
ACS Omega 2022, 7, 23673−23684

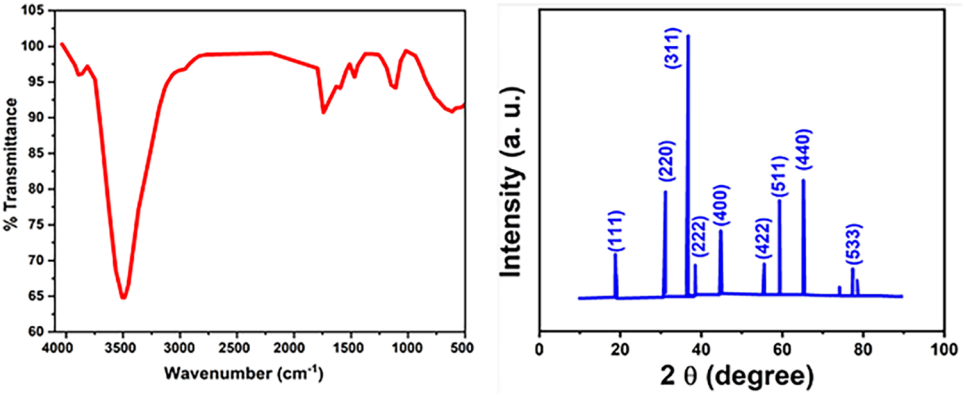

Figure 1. (a) FTIR and (b) XRD pattern of Co_3O_4-NPs fabricated by the marine red algae extract.

moieties. XRD analysis (PANalytical, Cu K radiation) was assessed to evaluate the crystallinity of Co_3O_4-NPs. A Shimadzu 2600 UV−vis spectrometer was used to estimate the typical and ideal wavelength and identify the prepared nanoparticles' absorption spectra. The surface morphology was examined by an FE-SEM (S-4800 HITACHI, Ltd., Japan). The particle shape and nanoparticle size of Co_3O_4-NPs were assessed using an HRTEM (JEOL JEM 2100F). Dynamic light scattering was used to evaluate the particle size via SZ-100, Horiba Scientific, Japan. The specific surface area and pore size were ascertained using a Brunauer−Emmett−Teller (BET) nitrogen adsorption−desorption apparatus (Micrometrics Instruments, USA-ASAP2020).

2.3.2. Electrochemical Measurements. The electrochemical properties of the AC material and nanocomposite material (AC/Co_3O_4) were investigated by cyclic voltammetry (CV), galvanostatic charge−discharge (GCD), and electrochemical impedance spectroscopy on an electrochemical workstation (VSP, biological) controlled by EC-lab software (EIS). To produce a homogeneous slurry, the working electrode was formed by blending the active material, carbon black, and poly(vinylidene fluoride), with the following ratio of 80:10:10, respectively. The slurry was coated onto a nickel sheet current collector and dried overnight at 70 °C in a vacuum oven. The measurements for the AC electrode and the nanocomposite electrode (AC/Co_3O_4) were performed at room temperature that used a standard three-electrode cell configuration with Ag/AgCl acting as a reference electrode and platinum wire serving as a counter electrode in an aqueous electrolyte of Na_2SO_4 (1 M).

3. RESULTS AND DISCUSSION

In general, algae-supported biosynthesis of nanoparticles in the presence of their extracts is combined with the precursor metal solution. Red algae contain reducing components such as fats, oils, carbohydrates, proteins, antioxidants, and pigments (phycobilins and chlorophylls).[8] The HPLC detection method was used to determine and quantify phenolic compounds in the red algae; for example, lanosterol contains a seven-carbon metabolite with two phenolic and one primary hydroxy group. These functional groups work in different steps: (i) nucleation by reducing cobalt ions into neutral atoms, (ii) particle growth formation leads to the amalgamation of nucleated cobalt ions into different sizes of thermodynamically stable nanoparticles, and (iii) termination phase of cobalt nanoparticles determines the morphology of cobalt based on different factors such as incubation time, temperature, used concentration, and adjusted pH.[36,37] The phenolic −OH and −COOH groups have a high propensity to react with metals.[38] During chelate formation, the hydrogen from the ortho position of the phenolic −OH group is removed, resulting in a semiquinone structure. The electron-losing property of ellagic acid produces the H^+ radical. As a result of this process, Co(II) is converted to a Co atom, and the product is nanosized owing to the capping effect.[38] Our results that are in line with previous results are the following.

Figure 1a represents the FTIR spectra of Co_3O_4 nanoparticles produced with the red algae extract over the range 4000−500 cm^{-1}. An FTIR spectroscopic approach provides an appropriate route to sort the functional groups of red algae extract biomolecules associated with the formation of Co_3O_4 nanoparticles and is effective in shaping the nanoparticles to determine the capping agent. Different detected IR bands contributed to the nature of other functional groups in the red algae extract based on surface binding characteristics and played a vital role in the nanoparticle formation, such as 3500, 1669, 1413, and 1079 cm^{-1}. So, a broad peak of about 3500 cm^{-1} is the characteristic peak of alcoholic, polyphenol, and carboxylic groups, which belong to the primary and secondary amines and amide groups due to the stretching OH−NH bending.[39] The peaks at 1669, 1413, and 1079 cm^{-1} indicate aromatic rings in plant bending of −OH and C−O stretching of alcohols and carboxylic acids, which are in charge of the formation of Co_3O_4 nanoparticles.[14] The peaks at 760 and 562 cm^{-1} in the spectrum of Co_3O_4 nanoparticles are associated with Co^{+2} and Co^{+3} in a tetrahedral hole vibration in the spinel lattice, respectively.[40,41]

Figure 1b depicts the normalized XRD spectrum via the dual rule of marine red algae extract that acts as a reductant and stabilizing agent. Peaks are approximately indexed to the cubic structure of Co_3O_4-NPs.[42] The major diffraction peaks are located at 2Θ = 18.7, 31.1, 36.3, 38.6, 44.7, 55.2, 59.3, and 65.2°, which are assigned to the next crystal planes (111), (220), (311), (222), (400), (422), (511), and (440), respectively. The results for Co_3O_4-NPs were perfectly aligned with these significant peaks and matched with JCPDS #42-1467.[43] Here, the sharp peaks of Co_3O_4-NPs indicated good crystallinity, and no other phases or impurities were detected in the XRD, such as $\beta Co(OH)_2$ (JCDPS# 78-0431), confirming the high purity of the existing material, which may be attributed to the calcination effect, and the cobalt salt precursor was fully converted into Co_3O_4-NPs.These findings corresponded to the values found in the literature.[44] The average particle size was calculated using the Debye−Scherer equation, and the inner planar spacing was calculated using Bragg's law.[45] It is observed that the particle size of the formed nanoparticles is around 48 nm.

https://doi.org/10.1021/acsomega.2c02305
ACS Omega 2022, 7, 23673−23684

Figure 2 shows the UV spectrum of Co_3O_4-NPs studied at room temperature. UV−vis spectroscopy revealed two significant peaks of Co_3O_4-NPs found at 400 and 741 nm, respectively. These two different wavelengths may be due to the charge-transfer effect from the ligand to the metal as $O^{2-} \rightarrow Co^{2+}$ for the first absorption peak and $O^{2-} \rightarrow Co^{3+}$ for the second absorption peak at λ = 741 nm.[46] Around 400 nm, this peak was also assigned to the surface plasmon resonance behavior.[47] The green prepared Co_3O_4-NPs may be significantly greater than the above-reported value caused by the difference.[48] These peaks signified the transfer processes of Co(II) and Co(III) with oxygen.[49]

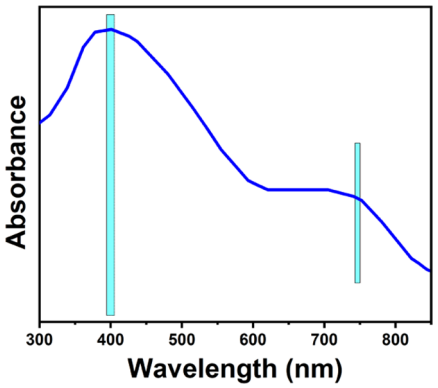

Figure 2. UV spectrum of Co_3O_4-NPs.

SEM characterized the morphological features and Co_3O_4-NPs of the marine red algae extract. Figure 3a,b depicts the SEM micrograph of red algae after the treatment protocol. Dried *G. sparsa* (red algae) are long, thin staples close together and have a complicated sheet-like structure with strong edges.[50] Triangular and rectangular diatoms occasionally surround the branches. SEM images of Co_3O_4-NPs at two different magnifications are listed in Figure 3c−e. The SEM texture demonstrates that the sample is composed of small spherical particles that freely accumulate in the presence of cluster nanoparticles formed by the aggregation of individual nanoparticles. The particles are uniform in size and noticeably distributed.[51] The manufacturing method has effectively addressed the agglomeration issues, and it is suitable for producing the smallest Co_3O_4-NPs whose exact particle size can be measured with SEM.[52]

The material's elemental composition was determined using energy dispersion microanalysis (high-resolution EDAX) (Figure 3f). EDAX analysis of Co_3O_4NPs was carried out from 0 to 20 keV, and the spectrum data displays Co and O as the significant elements with high intensity. It exhibited a peak of cobalt nanoparticles at 7 keV together with other small peaks. From the EDAX profile, a strong cobalt signal peak was confirmed.[53]

Figure 4a,b depicts the particle shape of Co_3O_4-NPs, and the particles appeared in spherical shapes,[54] with some aggregation owing to the secondary metabolite complex surrounded by the particles as a coating layer.[55] The spacing between the lattice fringes (d) for the as-prepared nanoparticles is 0.28 nm (Figure 4c), which is compatible with the (311) plane of Co_3O_4-NPs, as seen in the SAED image. Figure 4d shows the size distribution of Co_3O_4-NPs (48.1 ± 5.32 nm), which fit the obtained data from the TEM and XRD sections. Figure 4d illustrates the SAED of Co_3O_4-NPs, in which these bright spots constituted mainly five planes that also concur with the XRD graph.[56] Meanwhile, the dispersed rings with bright spots for Co_3O_4-NPs reflect the polynanocrystalline nature of the produced nanoparticles. Additionally, these bright spots reveal the crystalline structure.

The surface characteristic was measured by the N_2 adsorption isotherm using the BET method,[57,58] the most widely used procedure for determining the surface area of solid materials. The surface area of a nanocomposite is widely known to have a key role in developing high chemical reactivity. It could be

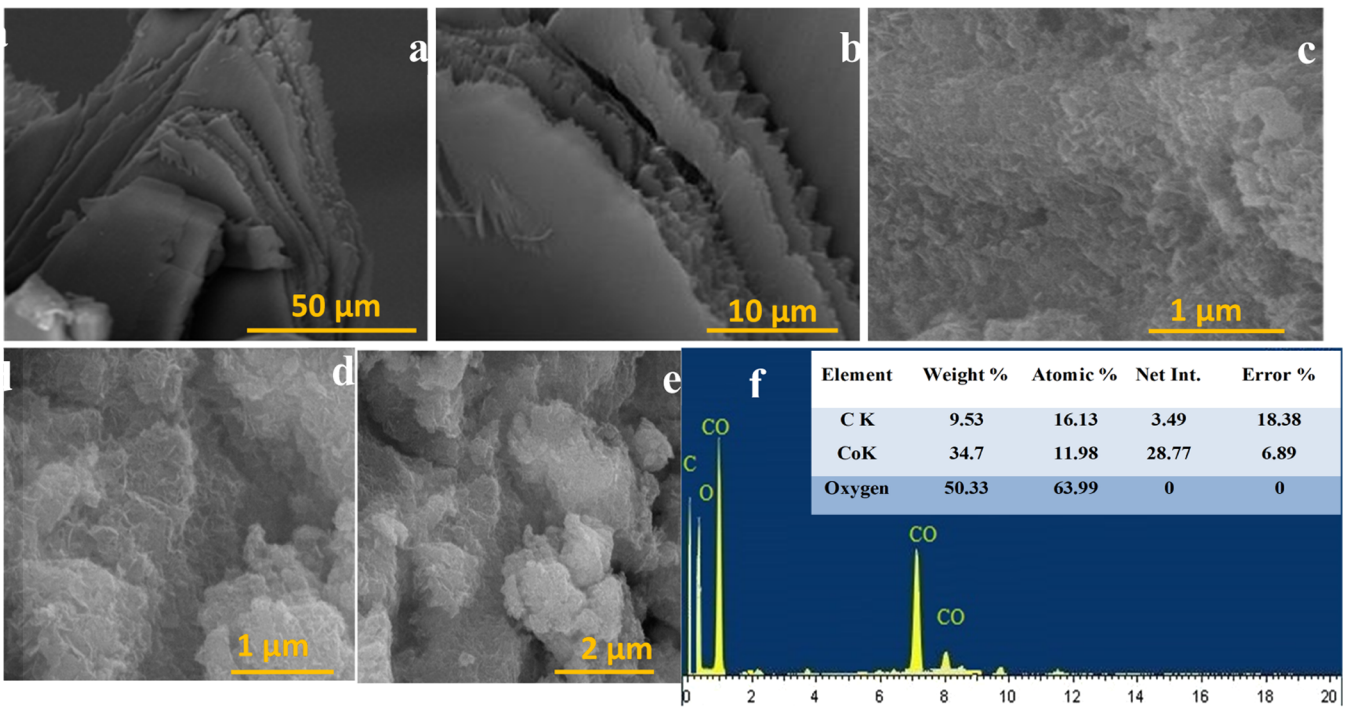

Figure 3. (a, b) SEM of marine red algae at different magnifications, (c−e) SEM of Co_3O_4-NPs, and (f) EDX.

https://doi.org/10.1021/acsomega.2c02305
ACS Omega 2022, 7, 23673−23684

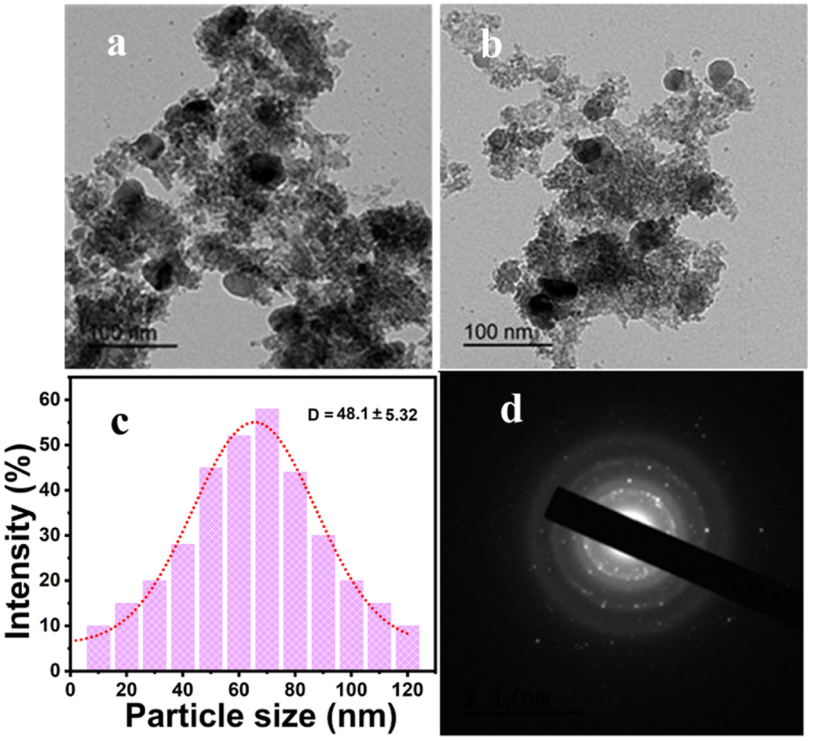

Figure 4. (a, b) TEM, (c) DLS, and (d) SAED of Co_3O_4-NPs.

noticed that nanoparticles might enlarge the adsorption capacity in their nanocomposite form.[57] The specific surface area of the nanocomposites is reported as 35.21 $m^2\ g^{-1}$ for Co_3O_4-NPs, as shown in Table 1 and Figure 5a,b. The formation of this nanocomposite form leads to the progression of surface area and is accompanied by additional porosity. The average particle radius is 51.44 nm. The average pore size is 8.03 nm. This may be due to the removal of water molecules during the phase transformation of β-$Co(OH)_2$ to Co_3O_4.[59]

Table 1. Variation of the BET Surface Area, Average Pore Size, and Average Particle Radius for Co_3O_4-NPs

chemical composition	average pore size (nm)	BET surface area ($m^2\ g^{-1}$)	average particle radius (nm)
Co_3O_4-NPs	8.03	35.21	51.44

3.1. Electrochemical Study. Cyclic voltammetry (CV) was considered to be a good tool for determining the change between non-Faradaic and Faradaic reactions.[60] With a potential range of 0−1 V and various scan rates (10−100 mV s^{-1}), CV curves for AC electrode materials and nanocomposite (AC/Co_3O_4) electrode materials on an electroactive area of 1 cm^2 are shown in Figure 6a,b. Regarding AC and AC/Co_3O_4, CV curves have a quasirectangle shape with two slight redox peaks. The CV curves indicate no visible distortion as the scan rate increases, providing high capacitive performance. They also contribute to developing specific capacitance as just a feature of scanning rates for AC materials and AC/Co_3O_4 nanocomposite materials. The specific capacitance (C_{sp}) of the AC and AC/Co_3O_4 electrodes decreases as the scanning rate increases.

Ions in the electrolyte have adequate time to access active sites in the electrode material at lower scan rates (10 mV s^{-1}),

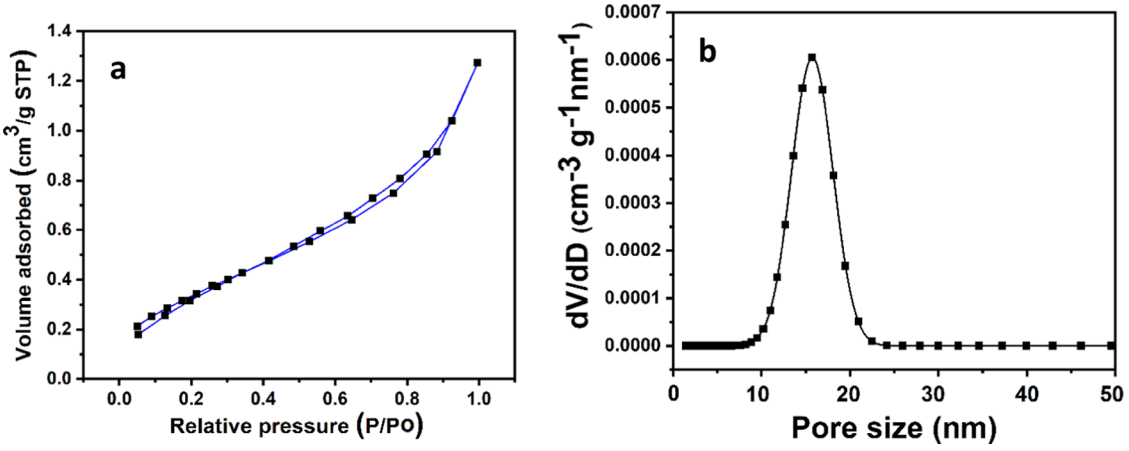

Figure 5. (a) N_2 adsorption/desorption isotherms of cobalt nanoparticles and (b) relative BJH pore size distribution.

https://doi.org/10.1021/acsomega.2c02305
ACS Omega 2022, 7, 23673−23684

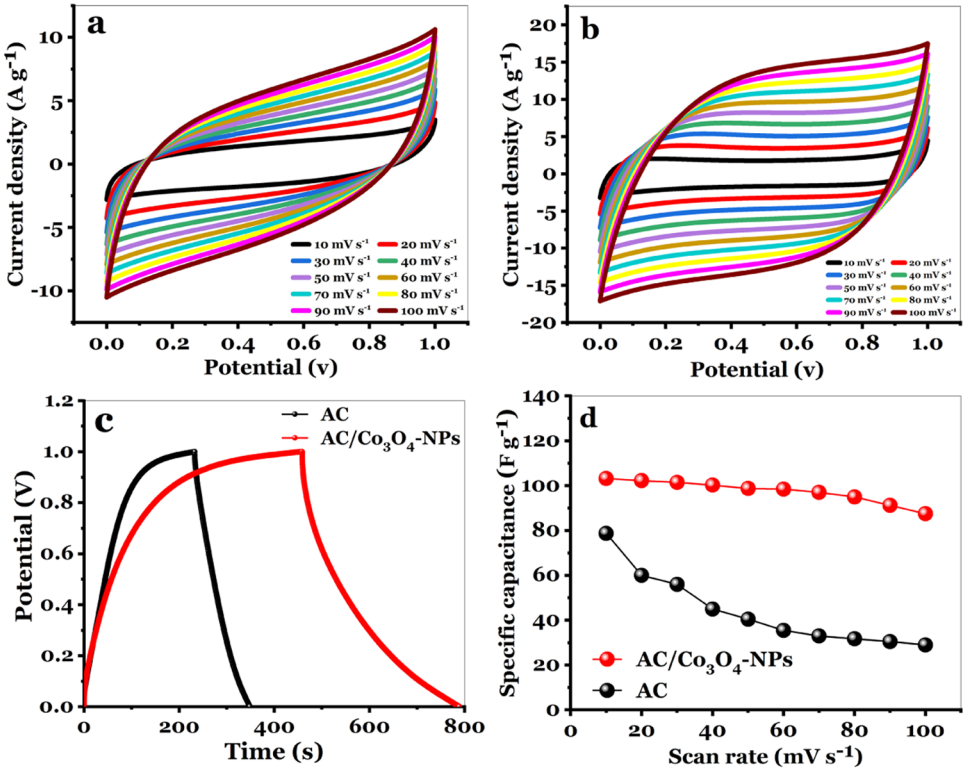

Figure 6. (a) CV curves of the AC electrode at different scan rates, (b) CV curves of the AC/Co_3O_4 nanocomposite electrode at different scan rates, (c) CV comparison for AC and AC/Co_3O_4 nanocomposite electrodes at a scan rate of 10 mV s^{-1}, and (d) calculated C_{sp} at different scan rates for AC and AC/Co_3O_4 nanocomposite electrodes.

resulting in a high specific capacitance. However, at higher scan rates, the electrolyte ions did not have enough time to reach the inside of the electrode, and only external surfactant sites could be used in the electrochemical reaction. The C_{sp} of the AC materials and AC/Co_3O_4 nanocomposite materials was calculated as follows

$$C_{CV} = \frac{Q}{m\Delta V} \tag{1}$$

where Q denotes the average charge, m (g) is the mass of the active material, and ΔV (V) is the potential window.

At scan rates (10 mV s^{-1}), Figure 6c compares CV curves with AC and AC/Co_3O_4 nanocomposite electrodes. Whenever the Co_3O_4 nanomaterial has been added to the AC material, the gained current area for the AC/Co_3O_4 electrode is significantly larger than that of the AC electrode, resulting in a higher specific capacitance for the nanocomposite (AC/Co_3O_4) electrode. As shown in Figure 6d, the specific capacitance C_{sp} determined from the cyclic voltammetry curves for the AC and AC/Co_3O_4 electrodes was 79.5 and 103.25 F g^{-1} at a scan rate of 10 mV s^{-1}, respectively.

GCD assessments were used to provide a complementary measurement of capacitance for the AC and AC/Co_3O_4 nanocomposite electrodes, conducted on the three electrodes at different current densities ranging from 1 to 5 A g^{-1} at a potential window (0−1 V). The charge curves for AC and AC/Co_3O_4 are nearly symmetric with their discharge counterparts. It is well recognized that the internal resistance (IR) drop demonstrates both the pseudocapacitive and double-layer contributions.

The AC and AC/Co_3O_4 have a minimum IR drop. The GCD profiles for the AC electrode and AC/Co_3O_4 nanocomposite electrode are shown in Figure 7a,b. The specific capacitance can be calculated using the following equation

$$C_{GCD} = \frac{I}{m\left(\frac{\Delta V}{\Delta t}\right)} \tag{2}$$

Figure 7c illustrates the GCD comparison for the AC electrode and the AC/Co_3O_4-NP electrode at a a current density of 1 A g^{-1} with an electroactive area of 1 cm^2. The C_{sp} of the AC/Co_3O_4 nanocomposite electrode is greater than that of the AC electrode, reflecting the influence of Co_3O_4-NPs on capacitance for the AC/Co_3O_4 electrodes. At a current density of 1 A g^{-1}, the C_{sp} values estimated from the GCD curves for the AC and AC/Co_3O_4 electrodes presented in Figure 7d are 125 and 182 F g^{-1}, respectively.

The energy density of the AC electrode is 17.36 and that of the AC/Co_3O_4 electrode is 25.27 Wh kg^{-1}. Furthermore, the power densities of AC and AC/Co_3O_4 electrodes are 543.44 and 585 W kg^{-1}, respectively.

The lower resistance examined by the EIS method at a range of frequency from 10 mHz to 100 kHz, and the applied amplitude of 10 mV may reflect the more incredible capacitive performance at high rates and the increment in the cycle stability of AC and AC/Co_3O_4 electrodes.[61] The spectra of the AC and AC/Co_3O_4 electrodes are divided into two parts in Figure 8a,b: one straight line due to the equivalent series resistor in the low-frequency region and the other semicircle due to the charge-transfer process at the electrode/electrolyte interface in the high-middle frequency region. The overall R_{ct} values of AC and AC/Co_3O_4 electrodes seem to be 10 and 2.9, respectively. At the same time, ESR values are 3.33 and 3.2 for such AC and AC/Co_3O_4 electrodes, respectively.

https://doi.org/10.1021/acsomega.2c02305
ACS Omega 2022, 7, 23673−23684

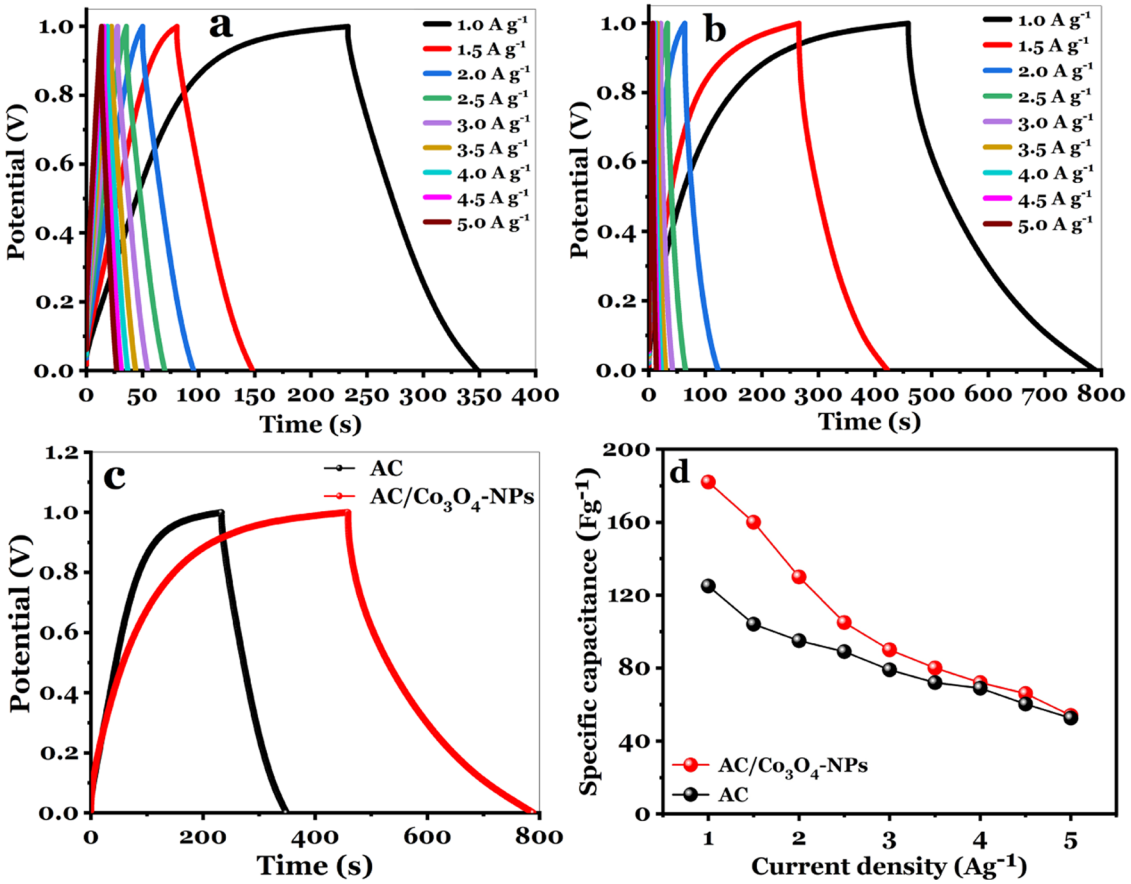

Figure 7. (a) GCD of the AC electrode at specific currents from 1 to 5 A g^{-1}, (b) GCD of the AC/Co_3O_4 nanocomposite electrode at specific currents from 1 to 5 A g^{-1}, (c) GCD comparison for AC and AC/Co_3O_4 nanocomposite electrodes at a current density of 1 A g^{-1}, and (d) calculated C_{sp} at a current density from 1 to 5 A g^{-1} for the AC and AC/Co_3O_4 nanocomposite electrode.

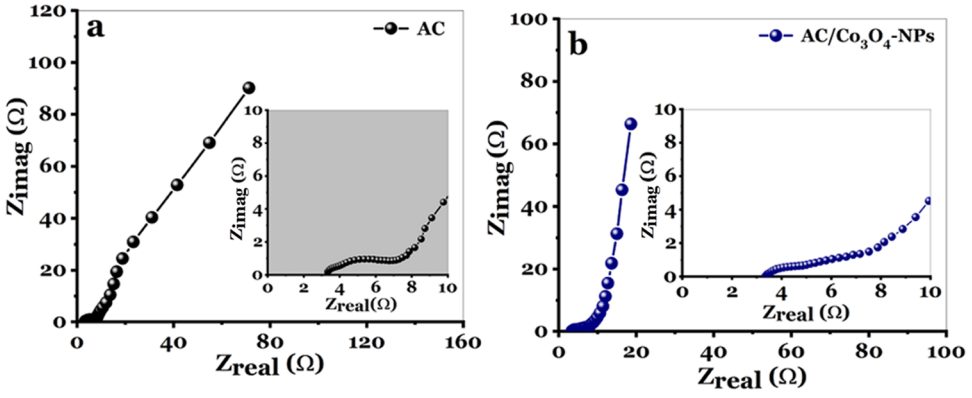

Figure 8. (a) Nyquist plots for the AC electrode developed with a 1 M Na_2SO_4 electrolyte and (b) Nyquist plots of the AC/Co_3O_4 nanocomposite electrode developed with a 1 M Na_2SO_4 electrolyte.

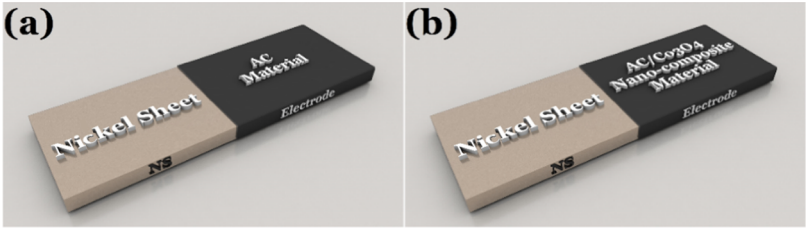

Figure 9. (a) Schematic design in 3D for the AC electrode and (b) schematic design in 3D for the AC/Co_3O_4 nanocomposite electrode.

https://doi.org/10.1021/acsomega.2c02305
ACS Omega 2022, 7, 23673−23684

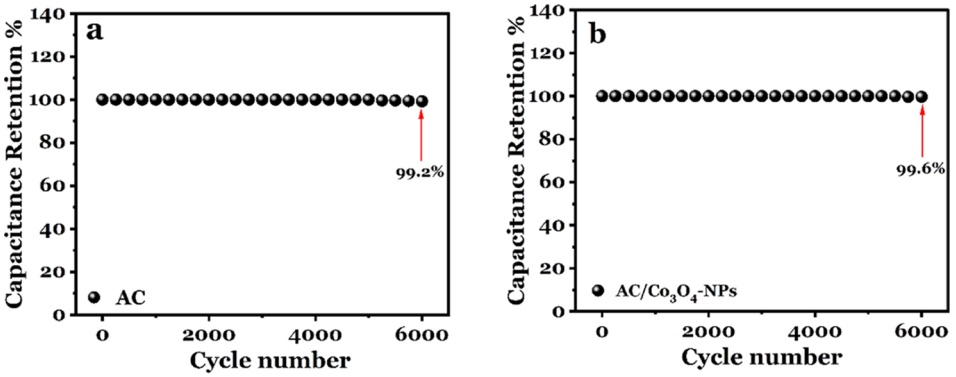

Figure 10. (a) Cycling stability and Coulombic efficiency over 6000 GCD cycles for the AC electrode and (b) cycling stability and Coulombic efficiency over 6000 GCD cycles for the AC/Co_3O_4 nanocomposite electrode.

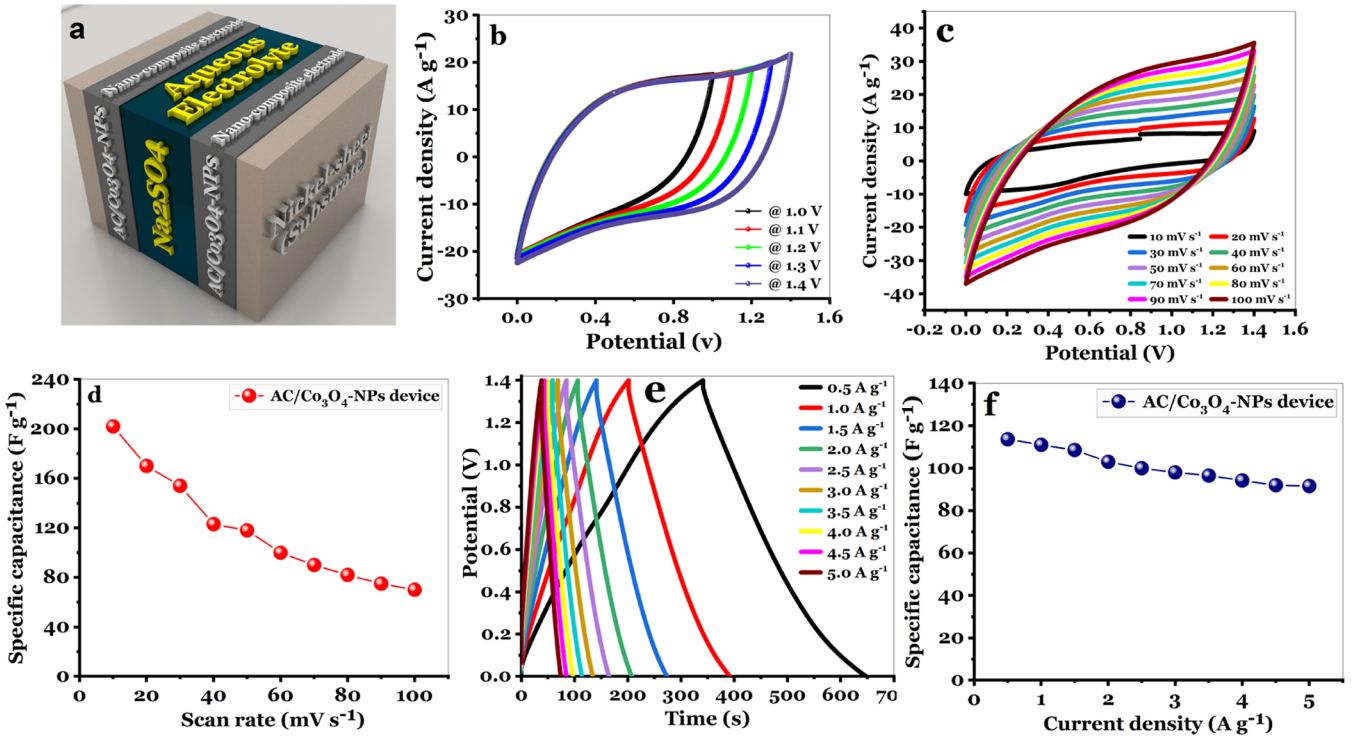

Figure 11. (a) Schematic design in 3D of the symmetric AC/Co_3O_4//AC/Co_3O_4 device, (b) CV curves for the symmetric AC/Co_3O_4-NP//AC/Co_3O_4-NP device in different potential windows at a scan rate of 50 mV s^{-1}, (c) CV curves at various scan rates for the symmetric AC/Co_3O_4//AC/Co_3O_4 device, (d) C_{sp} for the symmetric AC/Co_3O_4//AC/Co_3O_4 device with different scan rates, (e) GCD curves for the symmetric AC/Co_3O_4//AC/Co_3O_4 device at various specific currents, and (f) C_{sp} at specific currents from 0.5 to 5 A g^{-1} for the symmetric AC/Co_3O_4//AC/Co_3O_4 device.

The following equation can be used to calculate the specific capacitance

$$C_{EIS} = \frac{1}{2\pi m x f_{low} |Z_{imag}|} \quad (3)$$

where C_{EIS} (F g^{-1}) is the specific capacitance, f_{low} (Hz) is the low frequency, and Z_{imag} (Ω) is the magnitude imaginary impedance.

At a low frequency of 10 mHz, the specific capacitance (C_{sp}) estimated from the EIS method is 88.5 and 120 F g^{-1} for the AC and AC/Co_3O_4 electrodes, respectively. From these obtained data, AC/Co_3O_4 nanocomposite materials have a lower resistance value than AC materials, suggesting that AC exhibits the best electrical conductivity.

As observed in the schematic design shown in Figure 9a,b, the electrodes in the 3D presentation for an active material with a mass of 2 mg located on an area of 1 cm^2 for the AC and AC/Co_3O_4 electrodes are developed.

Continuous charge−discharge measurements were carried out for 6000 cycles at the same current density of 2.5 A g^{-1} as shown in Figure 10a,b for additional clarity and to evaluate the cycling stability of AC and AC/Co_3O_4 nanocomposite electrodes. It is observed that the AC electrode sustains 99.2% of its initial capacitance after 6000 cycles. On the other side, it is remarkable that 99.6% of the capacitance for the AC/Co_3O_4 electrode is maintained.

3.2. AC/Co_3O_4//AC/Co_3O_4 Symmetric Supercapacitor Device. The schematic illustration of an asymmetric AC/Co_3O_4 supercapacitor device established using AC/Co_3O_4 as the anode and cathode electrodes is displayed in Figure 11a. It can be seen that the two electrodes have the same size, with a mass of 8 mg and a surface area of 4 cm^2. The necessity of using a

https://doi.org/10.1021/acsomega.2c02305
ACS Omega 2022, 7, 23673−23684

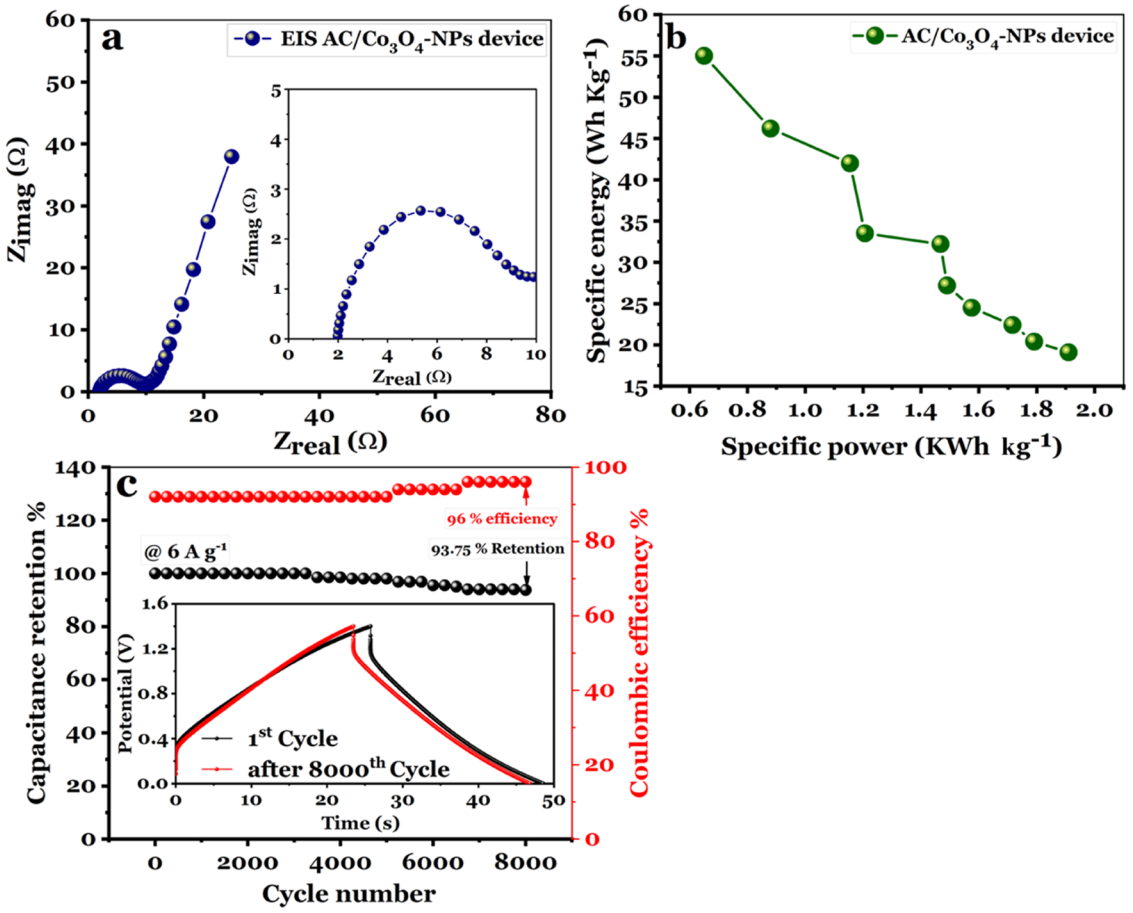

Figure 12. (a) Nyquist spectrum recorded for the symmetric $AC/Co_3O_4//AC/Co_3O_4$ device developed in a 1 M Na_2SO_4 aqueous electrolyte, (b) Ragone plot of the symmetric $AC/Co_3O_4//AC/Co_3O_4$ device, and (c) capacitance retention vs Coulombic efficiency with a cycle number for the symmetric $AC/Co_3O_4//AC/Co_3O_4$ device at 6 A g^{-1}.

Whatman filter paper as a separating material between the two electrodes was considered. On the other side, sodium sulfate (Na_2SO_4, 1 M) was also used as the aqueous electrolyte. Figure 11b depicts the CV curves for an asymmetric AC/Co_3O_4 supercapacitor device with a potential window extending from 0 to 1.4 V and a scan rate of 50 mV s^{-1}. As shown in Figure 11b, the value of specific capacitance C_{sp} for a symmetric AC/Co_3O_4 supercapacitor device decreases from 220 to 118 F g^{-1} at a scan rate of 50 mV s^{-1} as the voltage ranges from 1 to 1.4 V.

The curves show capacitive performance with a distortion-free quasirectangular curve with no firm redox peaks, even when the voltage increases by 1.4 V. Cyclic voltammetry curves of the symmetric $AC/Co_3O_4//AC/Co_3O_4$ supercapacitor device are shown in Figure 11c. The performance of the symmetric $AC/Co_3O_4//AC/Co_3O_4$ device was investigated at various scan rates from 10 to 100 mV s^{-1} with a voltage range (0−1.4 V); with a quasirectangular CV shape, the pseudocapacitive behavior was revealed. The shape of the CV curves almost stays the same as the scan rate is increased, showing that the constructed device has strong reversibility and rate capability and a decent working cell voltage. These findings indicate that Co_3O_4 NPs are a suitable electrode for supercapacitors, wherein the performance is further examined by various advanced tools.

At another scan rate, the symmetric $AC/Co_3O_4//AC/Co_3O_4$ device exhibited specific capacitances of 202, 118, and 70 F g^{-1} (Figure 11d). The GCD curves for current densities ranging from 0.5 to 5 A g^{-1} are shown in Figure 11e. The linear change of both potential and time reflects the capacitive features of the symmetric $AC/Co_3O_4//AC/Co_3O_4$ device. Meanwhile, Figure 11f demonstrates that the symmetric ($AC/Co_3O_4//AC/Co_3O_4$) supercapacitor device can produce high-rate discharge specific capacities (C_{sp}) of 113.6, 111, 103, 98, 94.2, and 91.6 F g^{-1} at 0.5, 1, 2, 3, 4, and 5 A g^{-1}, respectively.

The capacitance is more exceptional because of the redox-reaction-enhanced energy storage.[62] The pseudocapacitors have a lower conductivity, making the fast electron transport challenging to achieve at a high rate. As a result, unique electrode materials with all features that could result in the most impressive supercapacitor feature, including high electrical conductivity, high porosity, and high capacitance, should be developed.

The Nyquist plots in Figure 12a reveal a short semicircle radius and steep straight line, indicating rapid charge transport at the electrode/electrolyte interface for the current symmetric supercapacitor device. The ESR and R_{ct} values are 9 and 1.82, respectively. To assess the overall electrochemical properties of the symmetric ($AC/Co_3O_4//AC/Co_3O_4$) supercapacitor device, Figure 12b displays the Ragone plot of the energy and power density. It is also observed that GCD curves with a power density of 0.65 kW kg^{-1} reveal a high energy density of 55 Wh kg^{-1} for the symmetric device. Even at a high power density of 1.91 kW kg^{-1}, the symmetric system achieves a favorable energy density of 19.16 Wh kg^{-1}, implying its high capacity rate. The symmetric $AC/Co_3O_4/AC/Co_3O_4$ device's capacitance reten-

https://doi.org/10.1021/acsomega.2c02305
ACS Omega 2022, 7, 23673−23684

Table 2. Performance Comparison of our Supercapacitors with Other Symmetric and Asymmetric Supercapacitors

materials	SC type	electrolyte	voltage (V)	C_{sp} (F g^{-1})	ED (Wh kg^{-1})	PD (W kg^{-1})	retention	ref
Co_3O_4/VAGN/CF//Co_3O_4/VAGN/CF	symmetric	PVA/KOH gel	1	580	33	10 000	86.3% 20 K cycle	64
Co_3O_4/MnO_2/CC-90/AC	asymmetric	1 M KOH	2.2	616.7	54.71	1060	86.3% 10 K cycle	65
Co_3O_4/NiO//Co_3O_4/NiO	symmetric	3 M KOH	1.4	720.71	196	700	91.35% 5 K cycle	66
Co_3O_4//AC	asymmetric	KOH/PVA gel	1.5	60	16.25	7500	98.5% 2 K cycle	67
AC/Co_3O_4//AC/Co_3O_4	symmetric	1 M Na_2SO_4	1.4	125	55	650	93.75% 8 K cycle	this work

tion (retention %) and Coulombic efficiency (η%) are included in Figure 12c, obtained via conducting the cyclic charge/discharge test at a 1.4 V voltage window with a current density of 6 A g^{-1}. After 4000 GCD cycles, the symmetric device exhibits 98.5 and 92% capacitance retention and Coulombic efficiency. It is remarkable that the asymmetric device's capacitance retention and Coulombic efficiencies are 93.75 and 96%, respectively, after 8000 GCD cycles, implying that the asymmetric device is still acting as excellent delivers, which, in turn, demonstrates that the asymmetric device is still acting as exceptional cyclic performance.[63] These observations are in good accordance with the morphological characteristics and the electrochemical measurements. Co_3O_4-NPs with outstanding performance could be used for carbon textiles or activated carbon textiles to create flexible solid-state textile energy storage devices.

The electrochemical experiments demonstrate that the symmetric device constructed performed well and was stable. These findings indicate that Co_3O_4 might be used as a supercapacitor electrode material. Because of the usual and optimal architecture of the highly capacitive material, including the conductive layer and active contribution for pseudocapacitance, Co_3O_4-NPs were predicted to have improved electrochemical behaviors. The comparison between our supercapacitor findings and other symmetric and asymmetric supercapacitors is given in Table 2.

4. CONCLUSIONS

A simple protocol was rationally designed to prepare Co_3O_4-NPs based on abundant and natural marine red algae extract, resulting in a time- and energy-efficient process without harsh conditions. Based on FTIR spectroscopy, most likely surface-exposed carboxylic, amide, polyphenols, etc., are responsible for reducing, stabilizing, and inducing shaped nanoparticles. XRD determined the crystallinity of Co_3O_4-NPs, and the results were aligned with obtained significant peaks. The morphological properties showed that triangular and rectangular diatoms occasionally surround the branches of pure red algae and successfully make the size of produced nanoparticles uniform around 48.1 ± 5.32 nm. The BET surface area was assessed to be 35.21 m^2 g^{-1} with a pore size of 8.03 nm, reflecting the performance of the supercapacitor. The nanocomposite AC/Co_3O_4 exhibited a higher specific capacitance of 145.6% than raw AC materials.

The specific capacitance of AC/Co_3O_4 was 182 F g^{-1} at a current density of 1 A g^{-1} and 54 F g^{-1} at a current density of 5 A g^{-1}. It can also be concluded that the AC/Co_3O_4 nanocomposites showed high energy density and power density of 25.27 Wh kg^{-1} and 585 W kg^{-1}, respectively, at a current density of 1 A g^{-1}.

Interestingly, AC/Co_3O_4 exhibits remarkable cyclic stability, with the capacitance remaining almost constant (99.6%) after 8000 cycles at 2.5 A g^{-1}. According to the findings, the device achieved a capacitance retention of 93.75% with a Coulombic efficiency of 96%, demonstrating that the symmetric AC/Co_3O_4//AC/Co_3O_4 devices are appropriate for energy storage domains.

AUTHOR INFORMATION

Corresponding Authors

Mohamed M. Taher − *Department of Chemistry, Faculty of Science, Cairo University, 12613 Cairo, Egypt;* orcid.org/0000-0002-5032-9176; Email: m.taher923@gmail.com

Kamel Shoueir − *Institute of Nanoscience & Nanotechnology, Kafrelsheikh University, 33516 Kafrelsheikh, Egypt; Institut de Chimie et Procédés pour l'Énergie, l'Environnement et la Santé (ICPEES), CNRS UMR 7515, Université de Strasbourg, 67087 Strasbourg, France;* orcid.org/0000-0001-7994-559X; Email: kamel_rezk@nano.kfs.edu.eg

Authors

Badreah Ali Al Jahdaly − *Chemistry Department, Faculty of Applied Science, Umm Al-Qura University, Makkah 24382, Kingdom of Saudi Arabia*

Ahmed Abu-Rayyan − *Department of Chemistry, Faculty of Science, Applied Science Private University, Amman 11931, Jordan*

Complete contact information is available at: https://pubs.acs.org/10.1021/acsomega.2c02305

Author Contributions

The manuscript was co-written, co-revised, and co-prepared by all authors.

Notes

The authors declare no competing financial interest.

REFERENCES

(1) Hassaan, M. A.; Hosny, S. Green synthesis of Ag and Au nanoparticles from micro and macro algae-review. *Int. J. Atmos. Ocean. Sci.* **2018**, *2*, 10−22.

(2) Nguyen, T. M.-T.; et al. Biosynthesis of metallic nanoparticles from waste Passiflora edulis peels for their antibacterial effect and catalytic activity. *Arab. J. Chem.* **2021**, *14*, No. 103096.

(3) El-Desouky, N.; Shoueir, K. R.; El-Mehasseb, I.; et al. Bio-inspired green manufacturing of plasmonic silver nanoparticles/Degussa using Banana Waste Peduncles: Photocatalytic, antimicrobial, and cytotoxicity evaluation. *J. Mater. Res. Technol.* **2021**, *10*, 671−686.

(4) El-Naggar, M. E.; Wassel, A. R.; Shoueir, K. Visible-light driven photocatalytic effectiveness for solid-state synthesis of ZnO/natural clay/TiO2 nanoarchitectures towards complete decolorization of

https://doi.org/10.1021/acsomega.2c02305
ACS Omega 2022, 7, 23673−23684

methylene blue from aqueous solution. *Environ. Nanotechnol., Monit. Manage.* **2021**, *15*, No. 100425.
(5) Al Jahdaly, B. A.; Al-Radadi, N. S.; Eldin, G. M.; et al. Selenium nanoparticles synthesized using an eco-friendly method: dye decolorization from aqueous solutions, cell viability, antioxidant, and antibacterial effectiveness. *J. Mater. Res. Technol.* **2021**, *11*, 85−97.
(6) Shoueir, K. R. Green microwave synthesis of functionalized chitosan with robust adsorption capacities for Cr (VI) and/or RHB in complex aqueous solutions. *Environ. Sci. Pollut. Res.* **2020**, *27*, 33020−33031.
(7) El-Shabasy, R.; et al. A green synthetic approach using chili plant supported Ag/Ag2O@ P25 heterostructure with enhanced photocatalytic properties under solar irradiation. *Optik* **2019**, *192*, No. 162943.
(8) Khan, F.; Shahid, A.; Zhu, H.; et al. Prospects of algae-based green synthesis of nanoparticles for environmental applications. *Chemosphere* **2022**, *293*, No. 133571.
(9) Colin, J. A.; Pech-Pech, I.; Oviedo, M.; et al. Gold nanoparticles synthesis assisted by marine algae extract: Biomolecules shells from a green chemistry approach. *Chem. Phys. Lett.* **2018**, *708*, 210−215.
(10) Verma, S. K.; Panda, P. K.; Kumari, P.; et al. Determining factors for the nano-biocompatibility of cobalt oxide nanoparticles: proximal discrepancy in intrinsic atomic interactions at differential vicinage. *Green Chem.* **2021**, *23*, 3439−3458.
(11) Abbasi, B. A.; Iqbal, J.; Khan, Z.; et al. Phytofabrication of cobalt oxide nanoparticles from Rhamnus virgata leaves extract and investigation of different bioactivities. *Microsc. Res. Tech.* **2021**, *84*, 192−201.
(12) Khalil, A. T.; Ovais, M.; Ullah, I.; et al. Physical properties, biological applications and biocompatibility studies on biosynthesized single phase cobalt oxide (Co3O4) nanoparticles via Sageretia thea (Osbeck.). *Arab. J. Chem.* **2020**, *13*, 606−619.
(13) Iqbal, J.; Abbasi, B. A.; Batool, R.; et al. Biogenic synthesis of green and cost effective cobalt oxide nanoparticles using Geranium wallichianum leaves extract and evaluation of in vitro antioxidant, antimicrobial, cytotoxic and enzyme inhibition properties. *Mater. Res. Express* **2019**, *6*, No. 115407.
(14) Ajarem, J. S.; et al. Benign synthesis of cobalt oxide nanoparticles containing red algae extract: antioxidant, antimicrobial, anticancer, and anticoagulant activity. *J. Cluster Sci.* **2021**, *33*, 717−728.
(15) AlNadhari, S.; Al-Enazi, N. M.; Alshehrei, F.; et al. A review on biogenic synthesis of metal nanoparticles using marine algae and its applications. *Environ. Res.* **2021**, *194*, No. 110672.
(16) Rawat, S.; Mishra, R. K.; Bhaskar, T. Biomass derived functional carbon materials for supercapacitor applications. *Chemosphere* **2022**, *286*, No. 131961.
(17) Xu, M.; Huang, Q.; Lu, J.; et al. Green synthesis of high-performance supercapacitor electrode materials from agricultural corncob waste by mild potassium hydroxide soaking and a one-step carbonization. *Ind. Crops Prod.* **2021**, *161*, No. 113215.
(18) Surya, K.; Michael, M. Hierarchical porous activated carbon prepared from biowaste of lemon peel for electrochemical double layer capacitors. *Biomass Bioenergy* **2021**, *152*, No. 106175.
(19) Muhammad, A.; Jatoi, A. S.; Mazari, S. A.; et al. Recent advances and developments in advanced green porous nanomaterial for sustainable energy storage application. *J. Porous Mater.* **2021**, *28*, 1945−1960.
(20) Shinde, S. K.; Karade, S. S.; Maile, N. C.; et al. Green synthesis of novel CuCo2O4 nanocomposite for stable hybrid supercapacitors by deep eutectic solvents. *J. Mol. Liq.* **2021**, *334*, No. 116390.
(21) Maksoud, M. I. A. A.; Fahim, R. A.; Shalan, A. E.; et al. Advanced materials and technologies for supercapacitors used in energy conversion and storage: a review. *Environ. Chem. Lett.* **2021**, *19*, 375−439.
(22) Baldi, G.; Bonacchi, D.; Innocenti, C.; et al. Cobalt ferrite nanoparticles: The control of the particle size and surface state and their effects on magnetic properties. *J. Magn. Magn. Mater.* **2007**, *311*, 10−16.
(23) Jesudoss, S. K.; Judith Vijaya, J.; Iyyappa Rajan, P.; et al. High performance multifunctional green Co 3 O 4 spinel nanoparticles: photodegradation of textile dye effluents, catalytic hydrogenation of nitro-aromatics and antibacterial potential. *Photochem. Photobiol. Sci.* **2017**, *16*, 766−778.
(24) Adán-Más, A.; Silva, T.; Guerlou-Demourgues, L.; et al. Nickel-cobalt oxide modified with reduced graphene oxide: Performance and degradation for energy storage applications. *J. Power Sources* **2019**, *419*, 12−26.
(25) Rasheed, T.; Nabeel, F.; Bilal, M.; et al. Biogenic synthesis and characterization of cobalt oxide nanoparticles for catalytic reduction of direct yellow-142 and methyl orange dyes. *Biocatal. Agric. Biotechnol.* **2019**, *19*, No. 101154.
(26) Bibi, I.; Nazar, N.; Iqbal, M.; et al. Green and eco-friendly synthesis of cobalt-oxide nanoparticle: characterization and photocatalytic activity. *Adv. Powder Technol.* **2017**, *28*, 2035−2043.
(27) Hu, C.-C.; Chang, K. H.; Lin, M. C.; et al. Design and tailoring of the nanotubular arrayed architecture of hydrous RuO2 for next generation supercapacitors. *Nano Lett.* **2006**, *6*, 2690−2695.
(28) Ding, X.; Liu, R.; Zhao, J.; et al. In situ formation of Co 3 O 4 nanocrystals embedded in laser-induced graphene foam for high-energy flexible micro-supercapacitors. *Dalton Trans.* **2022**, *51*, 2846−2854.
(29) Yan, H.; Bai, J.; Liao, M.; et al. One-Step Synthesis of Co3O4/Graphene Aerogels and Their All-Solid-State Asymmetric Supercapacitor. *Eur. J. Inorg. Chem.* **2017**, *2017*, 1143−1152.
(30) Tan, Y.; Liu, Y.; Kong, L.; et al. Supercapacitor electrode of nano-Co3O4 decorated with gold nanoparticles via in-situ reduction method. *J. Power Sources* **2017**, *363*, 1−8.
(31) Zhou, Y.; Wang, C.; Chen, F.; et al. Synchronous constructing ion channels and confined space of Co3O4 anode for high-performance lithium-ion batteries. *Nano Res.* **2022**, DOI: 10.1007/s12274-022-4281-y.
(32) Yu, M.; Sun, Y.; Du, H.; et al. Hollow porous carbon spheres doped with a low content of Co3O4 as anode materials for high performance lithium-ion batteries. *Electrochim. Acta* **2019**, *317*, 562−569.
(33) Vijayakumar, S.; Ponnalagi, A. K.; Nagamuthu, S.; et al. Microwave assisted synthesis of Co3O4 nanoparticles for high-performance supercapacitors. *Electrochim. Acta* **2013**, *106*, 500−505.
(34) Anuradha, C. T.; Raji, P. Facile synthesis and characterization of Co3O4 nanoparticles for high-performance supercapacitors using Camellia sinensis. *Appl. Phys. A* **2020**, *126*, 164.
(35) Liu, Z.; Yu, M.; Wang, X.; et al. Sandwich shelled TiO 2@ Co 3 O 4@ Co 3 O 4/C hollow spheres as anode materials for lithium ion batteries. *Chem. Commun.* **2021**, *57*, 1786−1789.
(36) Hofer, S.; Hartmann, A.; Orfanoudaki, M.; et al. Development and Validation of an HPLC Method for the Quantitative Analysis of Bromophenolic Compounds in the Red Alga Vertebrata lanosa. *Mar. Drugs* **2019**, *17*, 675.
(37) Ajarem, J. S.; Maodaa, S. N.; Allam, A. A.; et al. Benign synthesis of cobalt oxide nanoparticles containing red algae extract: antioxidant, antimicrobial, anticancer, and anticoagulant activity. *J. Cluster Sci.* **2022**, *33*, 717−728.
(38) Bibi, I.; Nazar, N.; Iqbal, M.; et al. Green and eco-friendly synthesis of cobalt-oxide nanoparticle: Characterization and photocatalytic activity. *Adv. Powder Technol.* **2017**, *28*, 2035−2043.
(39) Elakiya, N.; Arulmozhiselvan, K. Characterization of substrates of growing media by Fourier transform infrared (FT-IR) spectroscopy for containerized crop production. *J. Appl. Nat. Sci.* **2021**, *13*, 35−42.
(40) Dewi, N. O. M.; Yulizar, Y.; Apriandanu, D. O. B. Green synthesis of Co_3O_4 nanoparticles using Euphorbia heterophylla L. leaves extract: characterization and photocatalytic activity. *IOP Conf. Ser.: Mater. Sci. Eng.* **2019**, *509*, No. 012105.
(41) Vennela, A. B.; et al. Structural and optical properties of Co3O4 nanoparticles prepared by sol-gel technique for photocatalytic application. *Int. J. Electrochem. Sci.* **2019**, *14*, 3535−3552.
(42) Liu, X.; Long, Q.; Jiang, C.; et al. Facile and green synthesis of mesoporous Co 3 O 4 nanocubes and their applications for supercapacitors. *Nanoscale* **2013**, *5*, 6525−6529.

https://doi.org/10.1021/acsomega.2c02305
ACS Omega 2022, 7, 23673−23684

(43) Deori, K.; Ujjain, S. K.; Sharma, R. K.; et al. Morphology controlled synthesis of nanoporous Co3O4 nanostructures and their charge storage characteristics in supercapacitors. *ACS Appl. Mater. Interfaces* **2013**, *5*, 10665−10672.
(44) Samuel, M. S.; Selvarajan, E.; Mathimani, T.; et al. Green synthesis of cobalt-oxide nanoparticle using jumbo Muscadine (Vitis rotundifolia): Characterization and photo-catalytic activity of acid Blue-74. *J. Photochem. Photobiol. B* **2020**, *211*, No. 112011.
(45) Kumar, C. G.; Mamidyala, S. K. Extracellular synthesis of silver nanoparticles using culture supernatant of Pseudomonas aeruginosa. *Colloids Surf., B* **2011**, *84*, 462−466.
(46) Barreca, D.; Massignan, C.; Daolio, S.; et al. Composition and microstructure of cobalt oxide thin films obtained from a novel cobalt (II) precursor by chemical vapor deposition. *Chem. Mater.* **2001**, *13*, 588−593.
(47) Vijayanandan, A. S.; Balakrishnan, R. M. Biosynthesis of cobalt oxide nanoparticles using endophytic fungus Aspergillus nidulans. *J. Environ. Manage.* **2018**, *218*, 442−450.
(48) Vijayanandan, A. S.; Balakrishnan, R. M. Photostability and electrical and magnetic properties of cobalt oxide nanoparticles through biological mechanism of endophytic fungus Aspergillus nidulans. *Appl. Phys. A* **2020**, *126*, 234.
(49) Chen, Y.; Peng, D. L.; Lin, D.; et al. Preparation and magnetic properties of nickel nanoparticles via the thermal decomposition of nickel organometallic precursor in alkylamines. *Nanotechnology* **2007**, *18*, No. 505703.
(50) Lucaci, A. R.; Bulgariu, D.; Popescu, M. C.; et al. Adsorption of Cu (II) Ions on Adsorbent Materials Obtained from Marine Red Algae Callithamnion corymbosum sp. *Water* **2020**, *12*, 372.
(51) Kaviyarasu, K.; Raja, A.; Devarajan, P. A. Structural elucidation and spectral characterizations of Co3O4 nanoflakes. *Spectrochim. Acta, Part A* **2013**, *114*, 586−591.
(52) Ai, L.-H.; Jiang, J. Rapid synthesis of nanocrystalline Co3O4 by a microwave-assisted combustion method. *Powder Technol.* **2009**, *195*, 11−14.
(53) Jahani, M.; Khavari-Nejad, R. A.; Mahmoodzadeh, H.; et al. Effects of cobalt oxide nanoparticles (Co3O4 NPs) on ion leakage, total phenol, antioxidant enzymes activities and cobalt accumulation in Brassica napus L. *Not. Bot. Horti Agrobot. Cluj-Napoca* **2020**, *48*, 1260−1275.
(54) Lu, Y.; Fan, D.; Chen, Z.; et al. Anchoring Co3O4 nanoparticles on MXene for efficient electrocatalytic oxygen evolution. *Sci. Bull.* **2020**, *65*, 460−466.
(55) Valan, M.; Manikandan, A.; Antony, S. A. A novel synthesis and characterization studies of magnetic Co3O4 nanoparticles. *J. Nanosci. Nanotechnol.* **2015**, *15*, 4580−4586.
(56) Zhu, H.; Song, X.; Han, X.; et al. Co3O4 nanosheets preferentially growing (220) facet with a large amount of surface chemisorbed oxygen for efficient oxidation of elemental mercury from flue gas. *Environ. Sci. Technol.* **2020**, *54*, 8601−8611.
(57) Lu, K.; Gu, T.; Zhang, L.; et al. POM-assisted coating of MOF-derived Mo-doped Co3O4 nanoparticles on carbon nanotubes for upgrading oxygen evolution reaction. *Chem. Eng. J.* **2021**, *408*, No. 127352.
(58) Naushad, M.; Ahamad, T.; Ubaidullah, M.; et al. Nitrogen-doped carbon quantum dots (N-CQDs)/Co3O4 nanocomposite for high performance supercapacitor. *J. King Saud Univ.-Sci.* **2021**, *33*, No. 101252.
(59) Meher, S. K.; Rao, G. R. Ultralayered Co3O4 for high-performance supercapacitor applications. *J. Phys. Chem. C* **2011**, *115*, 15646−15654.
(60) Randviir, E. P. A cross examination of electron transfer rate constants for carbon screen-printed electrodes using Electrochemical Impedance Spectroscopy and cyclic voltammetry. *Electrochim. Acta* **2018**, *286*, 179−186.
(61) Zhu, Y.-X.; Song, G. L.; Wu, P. P.; et al. A burnished and Al-alloyed magnesium surface with improved mechanical and corrosion properties. *Corros. Sci.* **2021**, *184*, No. 109395.
(62) Chandrasekaran, N. I.; Muthukumar, H.; Sekar, A. D.; et al. High-performance asymmetric supercapacitor from nanostructured tin nickel sulfide (SnNi2S4) synthesized via microwave-assisted technique. *J. Mol. Liq.* **2018**, *266*, 649−657.
(63) Sun, L.; Sun, Y.; Fu, Q.; et al. Facile preparation of NiO nanoparticles anchored on N/P-codoped 3D carbon nanofibers network for high-performance asymmetric supercapacitors. *J. Alloys Compd.* **2021**, *888*, No. 161488.
(64) Liao, Q.; Li, N.; Jin, S.; et al. All-solid-state symmetric supercapacitor based on Co3O4 nanoparticles on vertically aligned graphene. *ACS Nano* **2015**, *9*, 5310−5317.
(65) Liu, G.; Ma, L.; Liu, Q. The preparation of Co3O4@ MnO2 hierarchical nano-sheets for high-output potential supercapacitors. *Electrochim. Acta* **2020**, *364*, No. 137265.
(66) Hu, Q.; Gu, Z.; Zheng, X.; et al. Three-dimensional Co3O4@ NiO hierarchical nanowire arrays for solid-state symmetric supercapacitor with enhanced electrochemical performances. *Chem. Eng. J.* **2016**, *304*, 223−231.
(67) Chen, J.; Xu, Z.; Zhu, H.; et al. An ultrafast supercapacitor built by Co3O4 with tertiary hierarchical architecture. *Vacuum* **2020**, *174*, No. 109219.

https://doi.org/10.1021/acsomega.2c02305
ACS Omega 2022, 7, 23673−23684